Mirror-based Full-View Finger Vein Authentication with Illumination Adaptation

Junduan Huang, Zifeng Li, Sushil Bhattacharjee, Sébastien Marcel, Wenxiong Kang

***Abstract*—Full-view finger vein (FV) biometrics systems capture multiple FV images of the presented finger ensuring that the entire surface of the finger is covered. Existing full-view FV systems suffer from three common problems: large device size, high cost for multi-camera system, and sub-optimal illumination in the recorded FV images. To address the problem of device size, we propose a novel Mirror-based Full-view FV (MFFV) capture device. The MFFV device has a compact size by using mirror-reflection approach. We reduce the cost of the device by using low-cost components, in particular, consumer-grade cameras. To address the problems of lower-quality images captured by such cameras and obtain optimally illuminated FV images, we propose a two-step approach. The first step is a Multi-illumination Intensities FV (MIFV) capture strategy, which capture the FV image set with varying illumination intensities. In the second step, a FV illumination adaptation (FVIA) algorithm is proposed to select the optimally illuminated FV image from the MIFV image set. Using the proposed MFFV device, we collect a comprehensive dataset, namely MFFV dataset, along with reproducible baseline FV authentication results for both single-view and full-view FV. Our experimental results demonstrate that the MIFV capture strategy as well as the FVIA algorithm can effectively improve the authentication performance, and that the full-view FV authentication is significantly superior than the single-view FV authentication. The source-code and dataset for reproducing our experimental results are publicly available [1].**

***Keywords*—Biometrics, Vein recognition, Finger vein, Full-view, Authentication**

I. Introduction

Although vein biometrics has not been explored as extensively as some other biometrics modalities such as face and fingerprint modalities, the subject has increasingly attracted research attention in recent years [1–8]. Vein biometrics has the potential to be widely used [9, 10] as it offers several advantages. (1) Vein patterns are unique to every individual [9]. (2) As veins are located beneath the skin, vein patterns are difficult to counterfeit. (3) The vein-pattern imaging process uses near-infrared (NIR) illumination, and relies on the fact that NIR is more strongly absorbed by the blood in the veins than in the surrounding tissue. This phenomenon of differential absorption is seen only in living bodies, and therefore can be used for liveness detection [9].

The most commonly studied vein biometrics traits are eye vein patterns and hand vein patterns. Eye vein biometrics includes sclera vein and retinal vein biometrics. Hand vein biometrics, mainly for palm vein, dorsal hand vein, wrist vein, and finger vein (FV) biometrics, are more commonly used than eye vein biometrics. There are two reasons for this: (1) hand vein biometrics systems are less intrusive than eye-vein biometrics systems, and (2) different hand vein traits can be combined (fused) together in a straightforward way, to construct more robust vein biometrics systems [11–13]. In other words, compared to other vein-biometrics modalities, the advantages of hand-vein biometrics are convenience and acceptability.

In hand vein biometrics, up to now the main emphasis has been on developing feature-extraction methods. Many novel computer vision and image processing methods have been proposed for improving the feature extraction ability of vein biometrics systems [1–8]. In contrast, not many works have been published on vein-imaging approaches.

Since biometric traits in the different flavors of hand vein biometrics (*e.g.*, wrist vein, palm vein, and FV) are very similar, feature-extraction and vein pattern authentication methods developed for one modality can be easily applied to the other hand vein modalities [11]. However, FV biometrics offers a distinct advantage: it is easier to realize multi-view or 3D capture, due to the smaller size of the target (fingers) compared to other modalities such as palm vein and wrist vein modalities. This advantage of FV modality brings several very useful benefits for biometrics authentication:

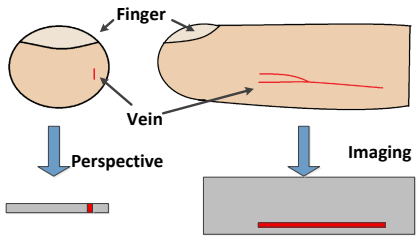

Fig. 1: Schematic diagram of finger vein self-occlusion. For intuitive observation, only one vein with self-occlusion is shown here. Here we assume that the veins analyzed are close to the imaging side, i.e. the part that is not heavily scattered.

This work was supported in part by the National Natural Science Foundation of China under Grant 61976095 and Grant 62376100 and in part by the Science and Technology Planning Project of Guangdong Province under Grant 2018B030323026. (Corresponding author: Wenxiong Kang.)

Junduan Huang is with School of Artificial Intelligence, South China Normal University, Foshan, 528225, China; and School of Automation Science and Engineering, South China University of Technology, Guangzhou, 510641, China; and Biometrics Security and Privacy Group, Idiap Research Institute, Martigny, 1920, Switzerland. (Email: runrunjun@163.com).

Zifeng Li, and Wenxiong Kang are with School of Automation Science and Engineering, South China University of Technology, Guangzhou, 510641, China. (e-mail: lizifeng01@qq.com; auwxkang@scut.edu.cn).

Sushil Bhattacharjee, Sébastien Marcel are with Biometrics Security and Privacy Group, Idiap Research Institute, Martigny, 1920, Switzerland. (e-mail: sushil.bhattacharjee@idiap.ch; sebastien.marcel@idiap.ch).

[1] The code and the license for MFFV-N dataset can be accessed at: https://github.com/SCUT-BIP-Lab/MFFV.

1) Multi-view FV samples not only contain more vein information but also compensate for distortions of veins near finger-borders, as well as for self-occlusion during FV imaging. Figure 1 schematically illustrates the problem of self-occlusion when using single-view imaging. This problem can be avoided by using multi-view imaging.
2) Multi-view FV authentication (FVA) significantly increases the difficulty of constructing presentation attacks (PA). As multi-view FV biometrics samples contain more comprehensive information than a single-view sample, a multi-view sample is more difficult to replicate accurately, because the attacker not only needs to acquire FV images from more viewpoints, but also capture the relationships among the multiple views.
3) Multi-view FVA can inherently handle the *pose variation* problem [14]. Pose variations, caused by translation or rotation of finger, introduce differences between enrolment and probe samples of the same finger, thus lowering the degree of match during FVA. Multi-view FVA systems capture more comprehensive FV information than single-view FV systems, which can be used to make the FV system pose-invariant.

Motivated by these advantages, many biometrics researchers are now exploring multi-view FV biometrics. There are three kinds of multi-view FV modalities:

1) **Partial multi-view modality** includes FV images from different views, but the images do not cover the entire finger [15, 16].
2) **Full-view** FV devices ensure that a given FV sample includes images covering the entire surface of the presented finger [14, 17–20].
3) In the **3D modality**, the 3D shape of the vein structures in the finger is reconstructed from a full-view FV sample [14, 19]. The 3D FV modality is an advanced version of full-view FV modality and all 3D FV devices also support full-view FVA without 3D reconstruction.

In table I we show the currently existing multi-view FV devices organized according to this taxonomy. The study of multi-view FV biometrics is still in the nascent phase, and several open problems remain in multi-view FV imaging:

1) *Large size of image capture device*: Existing works on multi-view FV systems can be grouped into two main categories: *multi-camera based design* [14, 15, 19] and *moving-camera based design* [17, 18]. Both designs suffer from the problem of large size. Multi-camera devices need more room for positioning several cameras (and their support) at reasonable distances and angle from the target (finger). Moving-camera devices need extra space to house the motor and other mechanisms for moving the camera along a fixed path. When comparing multi-view FV devices to the traditional single-view FV devices, especially in scenarios that require limited size, the disadvantage of large size cannot be ignored.
2) *Imaging problem due to finger thickness variations*: The quality of the captured FV image varies with light intensity and finger thickness. Under a fixed illumination intensity, images of different fingers may be underexposed or overexposed, depending on the finger-thickness. When capturing FV images from different angles, this problem is further accentuated by the fact that the cross-section of the finger is not perfectly circular. Consequently, under illumination with a fixed intensity, images of different fingers (or even of the same finger but from different angles) may be either underexposed or overexposed.
3) *High cost of multi-camera systems*: High image quality in FV images is usually achieved by using expensive, high performance cameras. This increases the cost of the FVA devices, even more so for multi-view FV systems. Using a single moving camera may reduce the camera cost, but increases the cost of the device in other ways, due to the additional systems required for rotating the camera accurately[2].

To promote the development of multi-view FVA, the aforementioned issues should be solved. In this work, we propose the following solutions to address these challenges: **First, to reduce the overall size of the multi-view FV device, we propose a novel mirror-based imaging method.** By using mirror-reflection, we propose here a compact full-view FV device, named Mirror-based Full-view FV (MFFV) device. The mirror-based design helps reduce the device size while maintaining adequate imaging distance. Using the MFFV device, we have collected a comprehensive FV dataset. This dataset shall be publicly shared with this work for scientific research. **Second, to address both the appropriate light intensity requirement for different finger thicknesses/angles and the cost-performance trade-off, we propose a Multi-illumination Intensity FV (MIFV) capture strategy and a corresponding FV Illumination Adaptation (FVIA) algorithm.** Specifically, during FV image capture, each camera records multiple FV images with different illumination intensities. Then, for each view, only the image with the best quality is chosen for further processing by using the proposed FVIA algorithm. That is, this work proposes a approach that combines a multi-illumination imaging strategy with a FV image quality assessment algorithm. The proposed approach addresses two issues in FV biometrics: first, it selects the appropriate light intensity requirement for different finger thicknesses and different views; and second, it is a software solution for achieving high image-quality even using low-cost cameras.

Our main contributions are:

1) A new design of a full-view FV imaging device. The proposed MFFV device has the advantage of low-cost and compact size for capturing full-view FV images.
2) The MFFV dataset[1]. Using the proposed MFFV device, we have collected a new full-view FV dataset that includes 127,800 images corresponding to 320 fingers.
3) A MIFV capture strategy and a corresponding FVIA algorithm. The combination of MIFV capture strategy and FVIA algorithm addresses the illumination intensity issue in FV imaging. This approach is an effective solution for improving the cost-performance ratio of FV imaging system.

[2]This cost-performance trade-off is one of the main reasons that adoption of multi-view FVA systems has been slow.

TABLE I: Taxonomy of multi-view FV studies. The literature on multi-view FV biometrics can be grouped into three kinds of modalities: partial multi-view FV, full-view FV and three-dimension (3D) FV. Note that the 3D FV is an advanced version of full-view FV and its device can also do full-view FV. The pictures of previously published multi-view FV devices shown in this table have been taken from the papers cited in the respective captions.

Taxonomy of Multi-view FV Biometrics Devices

Partial multi-view FV	**Full-view FV**		**Three-dimensional (3D) FV**
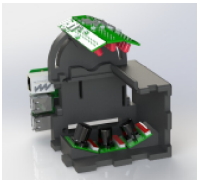	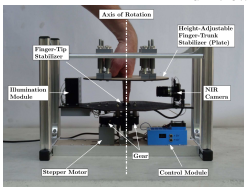	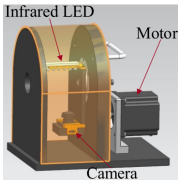	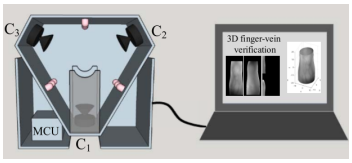
(a) Rozendal [15]	(c) Prommegger *et al.* [17]	(d) Qin *et al.* [18]	(g) Kang *et al.* [14]
	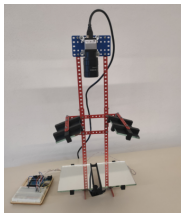		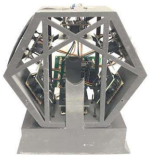 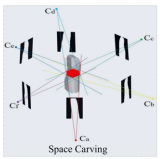
(b) Zhao *et al.* [16]	(e) Kauba *et al.* [20]	(f) **Proposed in this work**	(h) Yang *et al.* [19]

4) Reproducible baseline results[1] for the MFFV dataset. We present a comprehensive set of experiments to evaluate and demonstrate the effectiveness and the performance of all the proposed FVIA algorithm, and both the single-view and full-view FVA baselines.

The rest of this paper is organized as follows. The related works are discussed in Section II.The proposed MFFV device and the corresponding dataset are described in Section III. In Section IV, we present the design and the corresponding explanation of the FVIA algorithm. Experimental results are presented in Section V, in which the effectiveness of the proposed methods is evaluated by the rigorous experiments. Finally, we present our conclusions in Section VI.

II. Related works

In this section we mainly discuss previous works on multi-view FVA systems, analyzing their differences and pointing out their advantages and disadvantages. Then, some works on FV feature extraction and FV image quality assessment are briefly discussed.

A. Multi-View FV Imaging Systems

Different from the commonly used single-view based FVA, the multi-view approach attracts biometrics researchers due to its unique advantages: more information, more difficult to spoof, and more robust to pose variations. There are some excellent pioneering explorations for multi-view FVA. In Table I we illustrate previously proposed multi-view FV systems, alongside the device proposed in this work. The source publication for each device is indicated in the corresponding caption.

Rozendal [15] and Zhao *et al.* [16] have proposed partial multi-view FV image capture devices that capture FV images from only one side of the finger (devices (a) and (b) in Table I, respectively). These devices do not capture full-view FV patterns.

Prommegger *et al.* [17] (device (c) in Table I) and Qin *et al.* [18] (device (d) in Table I) have proposed full-view FV imaging devices. Both these devices are based on the moving-camera design. Besides the longer time required to record the full set of FV images sequentially, the moving camera design also requires expensive motor control circuitry to position the camera at specific positions with high precision.

Kang *et al.* [14] (device (g) in Table I) and Yang *et al.* [19] (device (h) in Table I) have proposed a multi-camera based approach to capture full-view FV images, which avoid the problems of the moving camera design. The main idea in these works is to mount multiple cameras around the finger so that the finger can be imaged from all directions. A minimum of three cameras is required to capture full-view FV samples because cameras set 120° apart are sufficient to cover the full view of the finger [14]. Yang *et al.* have also published a multi-view FV dataset (LFMB-3DFB) collected using their proposed device. As we shall see later, for the dataset collected in the present work all volunteers have presented fingers at specific orientations. Thus, for example, in the normal position (0° orientation), the View 3 ('bottom view'), all FV images in the dataset show the palmar view of the finger. By contrast, in the LFMB-3DFB dataset the different volunteers presented their fingers at arbitrary orientations. Consequently, for a given camera-view, all FV images do not correspond to the same orientation of the finger. Due to this difference, the FVA pipeline used in this work is not suitable for the LFMB-3DFB dataset.

However, these multi-camera systems also suffer from the following problems: the higher cost of additional cameras, and the space required for mounting cameras at different angles. Recently, Kauba *et al.* [20] (device (e) in Table I) have proposed a device employing a mirror based design to capture full-view FV images using only one camera and two mirrors. In their work, they explore three mirroring modes. Nevertheless, certain problems exist: their system suffers from insufficient depth of

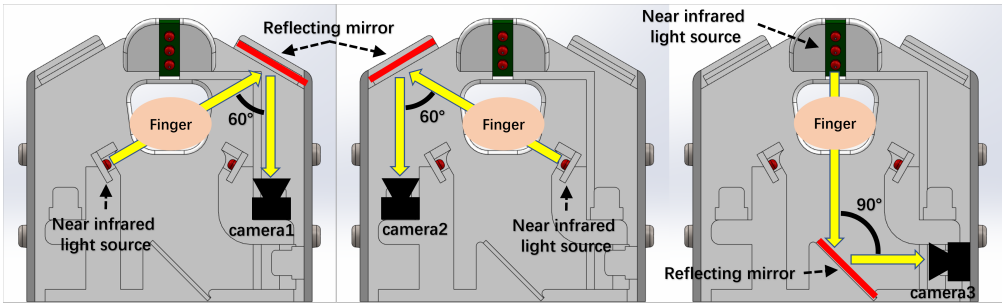

Fig. 2: The internal structure of the mirror-based imaging mechanism. For each view's FV imaging, the light passing through the finger is reflected by a dedicated mirror into the corresponding camera.

field, due to which fingers presented at different distances may be out of focus. In other words, using their device it is difficult to capture clear images from all views.

B. FV Feature Extraction

FV biometrics is based on the discrimination of vein patterns. The early works in FV biometrics focused mainly on extracting handcrafted features from single-view FV images, such as maximum curvature (MC) [21], repeated line tracking (RLT) [22], and wide line detector (WLD) features [23]. These feature-extraction methods as well as the Miura Matching (MM) score computation method [21] are well known in the field of FV biometrics, and several public-domain implementations are available [3] [4].

Inspired by the excellent performance of learning-based methods in recent years, the mainstream of FVA is increasingly moving towards deep-learning. Many new technologies or custom machine-learning models have been proposed.

Li *et al*. [24] propose an adaptive discriminant and sparsity feature descriptor (DSFD) for FV feature extraction. They first construct a direction difference vector (DDV) for representing the FV direction feature. Then, the DSFD adaptively projects the DDVs into a feature space, with discriminatory binary codes, in which the intra-class distance is minimized and the inter-class distance is maximized simultaneously. By using convolutional attention mechanism, Huang *et al*. [7], Zhang *et al*. [25] and Liu *et al*. [26] design the FV feature-extraction models, namely JAFVNet (Joint Attention FV netwrok), the LCAModel (lightweight convolutional attention model) and the MMRAN (multiscale and multistage residual attention network), respectively. The main differences among these three attention-based models are: the JAFVNet mainly focuses on the combination of the spatial and channel attention; the LCAModel focuses on the introducing the convolutional block attention module (CBAM) to the lightweight design; whereas the MMRAN mainly focuses on the combination of the proposed fusion residual attention block (FRAB) and multistage residual attention connection (MRAC). Hou *et al*. [27] propose a Convolutional Auto-Encoder (CAE) based method to extract FV features. Their proposed CAE-based model consists of a FV encoder, which extracts high-level feature representations from raw image-pixels, and a decoder that outputs reconstructed FV images from the high-level feature code. Kuzu *et al*. [28] have proposed a FV recognition framework using convolutional neural networks (CNN) and recurrent neural networks (RNN). Their method processes the FV images captured on-the-fly using their proposed device. Das *et al*. [29] propose a CNN-based FV identification system using a five-layer network. The main purpose of this work is to investigate whether the CNN is able to achieve stable and highly accurate performance when dealing with FV identification. Their experiments show that it is possible to achieve rank-1 identification accuracy higher than 95% for the publicly available FV datasets included in their study. Huang *et al*. [5] first adopted the Transformer encoder for FV feature extraction. By analysing the working mechanisms of Transformer encoder and combining several novel local information enhanced technologies, they proposed a customised FV Transformer (FVT). Based on frequency domain analysis of the FV images, Huang *et al*. [10] propose a complex-convolutional module for extracting FV feature in the frequency domain. Furthermore, they combine it with the traditional spatial domain CNN and propose a novel frequency-spatial coupling network for FVA, called FVFSNet.

C. Vein Image Quality Assessment

Image quality is one of the main factors affecting the performance of FV biometrics system. Vein images are dominated by vein patterns, which carry mainly texture and structure information [30]. Therefore, FV image quality can be assessed using measures of information capacity. The most well understood FV image quality measures are variance [31–35], which is correlated with the contrast within an image; and entropy [31, 32, 34, 35], which measures the information capacity of the image. There is another basic measure that directly indicates the illumination intensity, the mean gray value [36].

Besides these, other measures for assessing FV image quality have also been proposed. Nguyen *et al*. [37] propose a point-based vein image quality measure. However, this method is not easy to use because some parameters need to be fine-tuned for optimal performance. Qin *et al*. [38] have proposed a deep-learning based image-quality measure. Their method, however, is also cumbersome to use as the process of training the deep network adequately is quite laborious and time-consuming.

[3] https://www.idiap.ch/software/bob/docs/bob/bob.bio.vein/stable/index.html
[4] http://www.mathworks.nl/matlabcentral/fileexchange/authors/57311

Inspired by the experience of the above pioneering explorations on multi-view FVA, in this work we present a novel MFFV system, incorporating the proposed MIFV capture strategy and FVIA algorithm, which addresses the issues in existing full-view FV biometrics.

III. The Proposed MFFV Device and the Corresponding Dataset

A. The Proposed MFFV Device

Table I(f) shows a picture of the MFFV device proposed in this work. The dimensions of this device are 100×80×144mm, making it the smallest by volume among current multi-camera based full-view FV imaging devices. Quantitatively, the volume of the MFFV device is 54% of the device of Kang *et al*. [14] (shown in Table I(g)) and 45% of the 3D finger imaging device of Yang *et al*. [19] (Table I(h)). Note that the MFFV device dimensions given here include the screen, whereas the sizes cited for the other two devices do not include the human machine interface (HMI). For further comparison, we summarize the dimensions of all the multi-view FV devices in Table II for which the size information is publicly available[5].

TABLE II: Summary of the multi-view FV devices sizes.

Device	Dimensions
Kang *et al*. [14]	82×164×158mm
Yang *et al*. [19]	68×182×205mm
Prommegger *et al*. [17]	258×325×455mm
Qin *et al*. [18]	190×180×160mm
Ours	100×80×144mm

The main components of the MFFV device are: a Raspberry Pi 4 computing platform (costing approximately USD 35 [6]); a 4.3 inch liquid crystal display (LCD) screen (about USD 20 [7]), which is used as the HMI; a rotatable slider (3D-printed, in-house), which has two functions: 1) it serves as a receptacle for the finger, and 2) it allows the finger to be rotated within the device to certain fixed angles. The finger fits snugly in the slider when placed in it. When the finger is rotated, the slider rotates with it, due to friction. The slider is designed such that when rotated, it naturally slots into the $\pm 60^\circ$ angular positions. Thus, the data with different finger orientation poses can be captured. These multi-orientation FV data can be used for research on finger-rotation-invariant FVA.

The key innovation in the proposed MFFV device is the mirror-based design of the FV imaging system. The main features of the mirror-based design are as follows.

1) **Components of the mirror-based full-view FV imaging system:** The MFFV imaging system consists of three plane mirrors, three banks of NIR LED (850 nm, each bank has three LEDs, price less than USD 0.1 [8]), and three low-cost consumer-grade USB cameras (with driver circuit board, total cost about USD 14 [9]), along with the supporting structure (3D-printed in-house).
2) **Imaging mode of the mirror-based full-view FV imaging system:** As indicated in the name, the imaging mode of MFFV device is based on the mirror-reflection approach. Figure 2 shows the details of the mirror-based approach. The three cameras are positioned so as to capture FV images of the presented finger from three different angles separated by 120°. For each view the light passing through the finger is reflected by a dedicated mirror into the corresponding camera. The mirror helps to reduce the size of the device, hence making it compact.

The other innovative design feature of the MFFV device is the MIFV image capture strategy. During image capture, the LED bank corresponding to a given camera illuminates the finger six times, with increasing levels of power. Based on preliminary experiments, the illumination intensity is controlled via pulse width modulation (PWM) with the impulse ratios of 20%, 35%, 50%, 65%, 80%, and 95%. The percentages refer to the ratio of the allowed maximum power rating of the NIR-LEDs used to illuminate the finger being imaged. Thus, for each finger presentation, six images with different illumination intensities are recorded by each of the three cameras in the proposed MFFV device.

The MIFV capture strategy is complemented by the proposed FVIA algorithm. Before FV feature extraction, the FVIA algorithm selects, for each view, one of the six FV images. The selected image is considered to have the optimal image-quality according to the FVIA algorithm. As discussed in Section I, most of the existing FV imaging devices (single-view and multi-view) illuminate the finger with a fixed illumination intensity. This approach is simple to implement, but can lead to over- or underexposure of the finger. Our MIFV strategy solves this problem by recording several images under varying intensities of illumination and then selecting the most appropriate image. Since capturing multiple finger vein images with different illumination intensities requires more time, the proposed MIFV method can be seen as a trade-off between time and image-quality. Specifically, each image capture reqiures 50 ms. Hence capturing the full-view FV images takes 150 ms. By using the MIFV capture strategy, it takes 900ms (150 ms × 6). This method trades time for higher FV image quality. However, a total sample-capture-time of less than 1 second is considered acceptable in most use-cases.

B. MFFV Dataset

Using the proposed MFFV device, a full-view FV dataset, named MFFV dataset, has been collected for this study. The steps involved in data collection are as follows.

1) Each volunteer is asked to arbitrarily select 1-4 fingers from the index and middle fingers of both hands, according to the person's convenience.
2) For every presentation, the volunteer puts the selected finger in the MFFV device, and FV images from three

[5]For the devices of Kang *et al*. and Yang *et al*., we directly measured the dimensions with the authors in SCUT-BIPLab.

[6]https://www.raspberrypi.com/products/raspberry-pi-4-model-b/?variant=raspberry-pi-4-model-b-1gb

[7]https://item.taobao.com/item.htm?spm=a1z09.2.0.0.32bb2e8dXB6ugw&id=611130109637&_u=4ujhmf9f273

[8]https://item.taobao.com/item.htm?spm=a1z09.2.0.0.32bb2e8dXB6ugw&id=611149558677&_u=4ujhmf98194

[9]https://item.taobao.com/item.htm?spm=a1z09.2.0.0.32bb2e8dXB6ugw&id=569094981802&_u=4ujhmf93297

different views are captured. Each view produces six images with different illumination intensities. The upper-left view in the device is named View 1, the upper-right view is named View 2, and the bottom view (in this case, the palmar view of the finger) is named View 3.

3) The volunteer is asked to present the finger at three orientation positions – 0°, 60° clockwise and 60° anticlockwise. As introduced in Section III, the MFFV device includes a rotatable slider in which the volunteer places the finger for a presentation. The volunteer is asked to rotate the finger clockwise or anticlockwise until the slider slots into a new position. This position corresponds to $\pm 60^\circ$ orientation with reference to the nominal position. Thus, the slider assists the volunteer to rotate the finger to certain fixed angular positions approximately. One FV sample (consisting of three views) is recorded at each orientation position of the finger.
4) The volunteer makes 10 presentations for each finger. The person is instructed to remove the finger from the MFFV device each time, before commencing the next presentation.

In this work, 210 volunteers contributed FV images during data collection. After data-cleaning, the MFFV dataset consists of 172,800 images corresponding to 320 fingers. Each finger was presented 10 times. During a given presentation, three orientation poses of the finger have been considered, and in each orientation pose six images with different illumination intensities have been recorded for each of the three views.

TABLE IV: Summary of the MFFV dataset

Attribute	Statistic
Orientation pose	3 (normal, 60° clockwise/anticlockwise)
View	3 (Finger palmar, 120° clockwise/anticlockwise)
Illumination	6 intensities
Number of Samples per Finger	10
Number of Fingers	320
Image size	320×240
Image format	.bmp
Images per finger	540
Total number of images	172,800

The key statistics of the MFFV are summarized in Table IV. The main advantage of this dataset is that it is a full-view FV dataset; in addition, this dataset also includes full-view FV data with variations in illumination intensity and finger-pose. The MFFV dataset can be used for several FV research directions, such cross-orientation-pose FVA, cross-illumination research, multi-illumination-intensity fusion research, orientation invariant research, illumination intensity robust research, illumination adaptation research, and multi-views or cross-views research, among other topics. For the experiments presented in this work (Section V), we have used only the subset of the MFFV dataset with the normal (0°) finger-pose, as illustrated in Table III. We refer to this subset as the MFFV-N dataset. It consists of 172,800/3 = 57,600 FV images.

IV. The Proposed FVIA Algorithm

In this section we describe the proposed FVIA algorithm. First we present the two principles that have guided us in designing this algorithm. The algorithm operates over a specific region of interest (ROI). After describing the choice of ROI, we discuss the various components of the algorithm and their influences.

A. FVIA Design Principles

Inadequate illumination intensity has always been an obstacle in capturing high quality FV images. Under low illumination intensity, the veins to be imaged are not sufficiently illuminated, and the resulting image is underexposed. When the illumination intensity is too strong, the resulting FV image tends to be overexposed. In both conditions the veins are not easily discernible. To the best of our knowledge, most publicly known designs of FV imaging systems today rely on a single, fixed intensity of illumination. This is clearly not well adapted to different kinds of fingers. Motivated by this consideration, we have proposed the MIFV imaging design in the MFFV device (Section III). Here we describe the proposed FVIA algorithm, which is the software counterpart to the MIFV imaging strategy. Before explaining the proposed FVIA algorithm we present the two principles that have guided the design of the FVIA algorithm.

1) The FVIA algorithm relies on straightforward and proven FV image quality measures. As mentioned in Section II-C, the most commonly used and effective FV image quality measures are based on entropy, variance, and mean gray value. Our proposed FVIA algorithm also relies on these three measures.

TABLE III: Examples of the MFFV dataset

	Illumination 1	Illumination 2	Illumination 3	Illumination 4	Illumination 5	Illumination 6
View 1	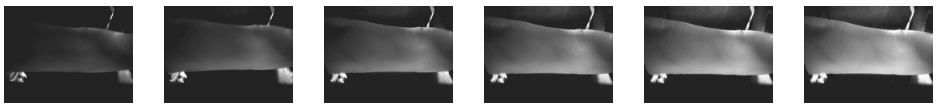					
View 2	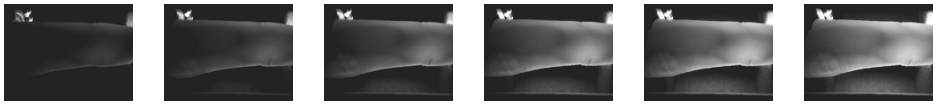					
View 3	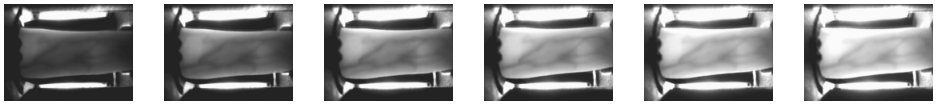					

2) We put forward the hypothesis that the mean gray value, $\bar{G}$, of the optimally illuminated images will lie in a specific range. The reasoning is as follows. The underexposed FV images have low mean gray value, while the overexposed FV images have high mean gray value. Both conditions are undesirable, as, in either case, the veins are not clearly imaged. The optimal illumination intensity lies somewhere between these two extremes.

Based on these design principles, a composite FVIA coefficient $\mathcal{C}$ is formulated in Equations 1, where i indicates the illumination intensity; E_i, V_i, and $\bar{G}_i$ denote the entropy, variance, and the mean gray value, respectively, of the input image corresponding to i; and T is a user-defined threshold. The function $\mathcal{F}_{FVIA}(E,\ V,\ \bar{G},\ T)$ is defined in Equation 2 and the normalization function $\mathcal{F}_N(\bar{G}, T)$ is given in Equation 3. The FVIA algorithm iterates over the illumination intensities with the predefined threshold, T, to select the FV image corresponding to the maximum value of $\mathcal{C}$.

$$\mathcal{C} = \arg\max_i \ \mathcal{F}_{FVIA}(E_i,\ V_i,\ \bar{G}_i,\ T) \tag{1}$$

$$\mathcal{F}_{FVIA}(E,\ V,\ \bar{G},\ T) = \frac{e^E + V}{\log\left(|\tanh\left(\mathcal{F}_N(\bar{G}, T)\right)| + 1\right)} \tag{2}$$

where

$$\mathcal{F}_N(\bar{G}, T) = \begin{cases} -\frac{\pi}{2}\left(\frac{T-\bar{G}}{T}\right)^2 - \frac{\pi}{6}, & \bar{G} \leq T \\ \frac{\pi}{2}\left(\frac{\bar{G}-T}{256-T}\right)^2 + \frac{\pi}{6}, & \bar{G} > T \end{cases} \tag{3}$$

In the following sections we discuss some key aspects of the FVIA algorithm.

B. ROI for FVIA

The captured FV images include some non-finger background, which not only influences the FV quality measurement, but also adds unnecessary computational load. Therefore, the coefficient $\mathcal{C}$ is computed over a predetermined ROI, which excludes image-regions that may correspond to background (non-finger region).

Based on the preliminary manual tests, we define that ROI as the central region of the FV, with dimensions 240 $\times$ 60. Table V shows an example of the ROI, for different illumination intensities and their corresponding component measures (E, V, $\bar{G}$). From the table we see that the values of E and V first increase and then decrease as the illumination intensity increases, whereas $\bar{G}$ keeps increasing with illumination intensity. This phenomenon is consistent with the analysis in Section IV-A.

TABLE V: Component measures used in the of FVIA algorithm, for different illumination intensities. E, V, and $\bar{G}$ denote the entropy, variance, and mean gray value, respectively. The measures have been computed for the chosen ROI, shown in the first column.

ROI for FVIA	E	V	$\bar{G}$
	5.747	236.243	70.371
	6.358	612.007	103.212
	6.590	825.434	133.148
	6.558	48.008	159.790
	6.587	8832.740	184.599
	6.251	768.766	204.149

C. The $tanh(\cdot)$-based design for using $\bar{G}$ in FVIA

In this section we discuss the construction of the denominator in Equation 2. To emphasize optimal illumination we would like the coefficient $\mathcal{C}$ to have low values for both overexposed and underexposed images, and higher values for the mid-range of illumination intensities. Therefore, the denominator in Equation 2 should take lower values as $\bar{G}$ tends towards the settable threshold, T, and higher values as the difference between $\bar{G}$ and T becomes larger.

We achieve this desired behavior by using the absolute value of the $tanh(\cdot)$ function in the denominator. For positive input values the response of $tanh(x)$ increases from zero (at $x = 0$) to the maximum value of 1 (as $x \to +\infty$) and the rate of increase gradually drops. While for the negative input value, it decreases from zero to the minimum value of -1. When using an absolute operation ($|\cdot|$) for the output of $tanh(x)$, its behavior satisfies our requirement for the denominator. By using this function in the denominator of the FVIA algorithm, we achieve the desired effect that $\mathcal{C}$ achieves its maximum value when the input (the input is constructed by $\bar{G}$, we discuss the input to the $tanh(\cdot)$ separately, in Section IV-D) near zero, and decreases for higher values of $\bar{G}$. Note that, when $\bar{G} = T$, then $(T - \bar{G})/T$ becomes zero. To avoid the $tanh(\cdot)$ function returning zero in this condition, we include a small offset (here we use π/6) in $\mathcal{F}_N(\cdot, \cdot)$.

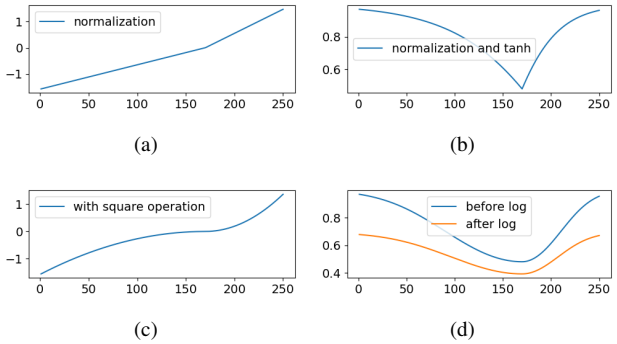

Fig. 3: Smooth-normalization of $\bar{G}$. Note that the threshold here is set to 170. (a) First normalization of $\bar{G}$; (b) Output of the first normalization of $\bar{G}$; (c) Smooth-normalization of $\bar{G}$; (d) Output of the smooth-normalization of $\bar{G}$.

D. Normalization for $\bar{G}$

In this section we discuss the construction of the function $\mathcal{F}_N(\bar{G}, T)$, as shown in Equation 3. This function forms the input of the $tanh(\cdot)$ function in the denominator in Equation 2, and takes the mean gray value, $\bar{G}$, and a user-defined threshold,

T, as arguments. In this way, the denominator in Equation 2 depends on $\bar{G}$ and its behavior can be regulated using the parameter T.

As explained in Section IV-A, the desired FV images should have a moderate (not extreme) mean gray value, $\bar{G}$. To achieve the desired behavior of the denominator, $\mathcal{F}_N(\bar{G}, T)$ should be small when $\bar{G}$ is close to the user-defined threshold T, and should produce higher-valued responses as $\bar{G}$ diverges from T (in both directions, higher as well as lower). This behavior can be achieved by simply normalizing $\bar{G}$ with respect to T, as shown in Equation 4.

$$N_{\bar{G}} = \begin{cases} -\frac{\pi}{2}\left(\frac{T-\bar{G}}{T}\right), & \bar{G} \leq T \\ \frac{\pi}{2}\left(\frac{\bar{G}-T}{256-T}\right), & \bar{G} > T \end{cases} \tag{4}$$

where the term $\pi/2$ is an arbitrary scaling factor. The operation in Equation 4 rescales $\bar{G}$ from range [0, 255] to the range [-π/2, π/2]. We note that when $\bar{G} = T$, $N_{\bar{G}} = 0$. At this point, $tanh(N_{\bar{G}})$ becomes 0. This condition can be avoided by adding a small arbitrary constant to $N_{\bar{G}}$. Here we use the value $\pi/6$ for this purpose.

We note, however, that there is an issue with Equation 4. To simplify the notation, let us define $X'(\bar{G}, T) = N_{\bar{G}} \pm \pi/6$ (when $\bar{G} \leq T$, it is -, otherwise it is +). The plot in Figure 3(b) shows the response of $tanh(X'(\bar{G}, T))$ as a function of $\bar{G}$, for a specific value of T (here, T=170). As we can see from this plot, the value of $tanh(X'(\bar{G}, T))$ drops sharply when $\bar{G}$ is close to the selected threshold T. This behavior is undesired, as it contradicts the common sense prior that the FV image with the $\bar{G}$ close to the optimal value should be considered as a high-quality image (*i.e.*, with high values for $\mathcal{C}$). We would like the denominator to vary smoothly, with $\bar{G}$, especially when $\bar{G}$ is near the pre-defined threshold T. We address this issue by using a square operation, to obtain the final version shown in Equation 3. In this way the $\bar{G}$ normalization influences the denominator in a smooth way, as shown in Figure 3(c).

E. Influence of Constituent Measures in FVIA

In this section the influence of each component in FVIA is explained graphically. The proposed FVIA algorithm relies on three measures: entropy, variance and mean gray value. In Equation 2 the mean gray value appears in the denominator, whereas the entropy and variance contribute to the numerator. In addition, as shown in Table V, these three measures exist in different scales. If we combine them directly using their raw values, the variance would dominate the other two variables in $\mathcal{C}$. To ensure comparable influence of all three measures, they should be transformed into the same range before being combined together.

We adopt some straightforward and effective mathematical operations to normalize the three constituent measures. First, to smooth the influence of mean gray value, the logarithm with margin is applied to the $tanh(\cdot)$ function. As Figure 3(d) shows, the logarithm operation makes the denominator smoother, which consequently has the effect of enlarging $\mathcal{C}$. Secondly, to increase the influence of the entropy with respect

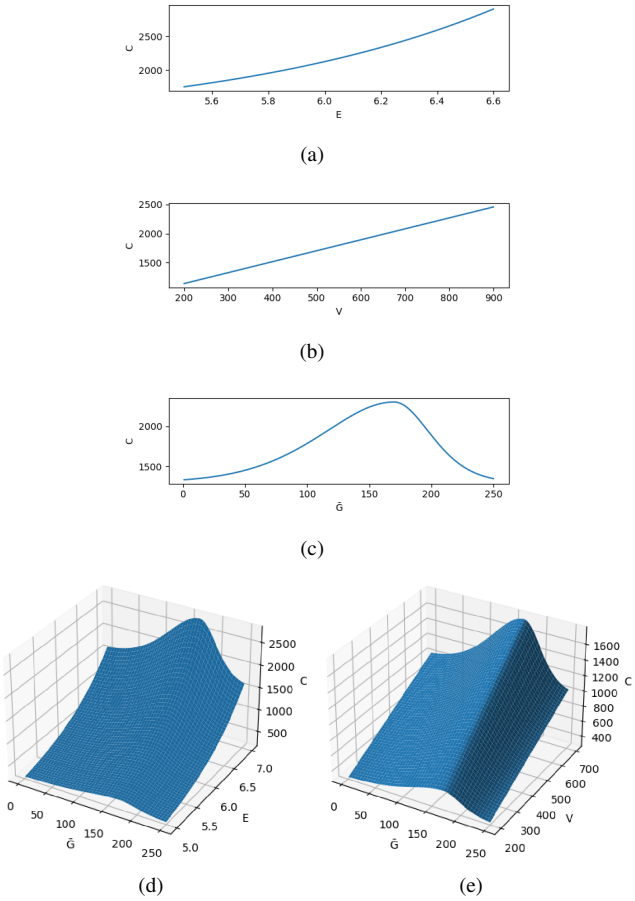

Fig. 4: Decoupling influence of the components in the proposed FVIA algorithm. Each plot in the figure shows the influence of one variable (indicated on the horizontal axis) on the image-quality coefficient $\mathcal{C}$ (on the vertical axis). In each plot the variables *not* being analyzed are set to an arbitrary default value: entropy to 4, variance to 500, mean gray to 135, while the threshold is set to 170. (a) Influence of entropy; (b) Influence of variance in FVIA algorithm; (c) Influence of mean gray in FVIA algorithm; (d) Influence of entropy with mean gray in FVIA algorithm; (e) Influence of the variance with mean gray in FVIA algorithm.

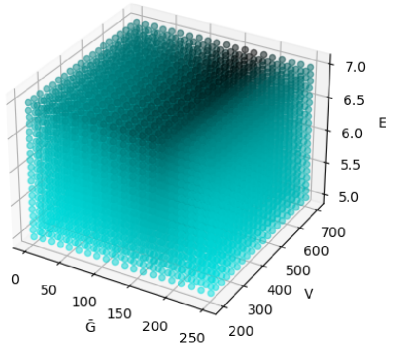

Fig. 5: The 4D plot of simulated results of the proposed FVIA algorithm. The three axes represent mean gray, variance, and entropy, respectively. The 4^{th} dimension is the color – the depth of the color indicates the value: the deeper, the larger.

to that of the variance, we consider the exponential of the entropy, as shown in Equation 2.

The plots in Figure 3(a)-3(c) show the influence of each constituent measure of C, decoupled from the other measures. From the figure it can be seen that the influences of these three components are on a similar scale. Note that $\mathcal{C}$ can be expressed as the sum of two parts – one part influenced only by the entropy, and the other part depending only on the variance. These two constituent parts are illustrated in as Figure 4(d) and 4(e). These plots demonstrate that the influences of these two parts are on the same scale. Final, the 4D plot of the whole FVIA algorithm is shown in Figure 5. We can see from the Figure 5 that the high scores (darker zones) of the FV images exist in the area where both entropy and variance values are large while the mean gray is close to the threshold. This result is consistent with the our requirement. Comprehensive experiments and further discussion of the proposed FVIA algorithm are presented in the Section V-D.

V. Experiments

In this section we describe the various experiments performed to evaluate the proposed methods. In particular, we have studied the properties of the proposed FVIA algorithm, as well as the FVA performance of the proposed MFFV device using a baseline FVA method. First, we describe the experimental protocols and the evaluation metrics. Then we describe the baseline FVA method used in this work. We present a comprehensive set of experiments to evaluate the proposed FVIA algorithm, following which we present baseline single-view and full-view FVA results for the MFFV-N dataset.

A. Experimental Protocols

In these experiments each finger is considered as an individual subject. The MFFV-N dataset is divided into three subsets: training set, development set, and test set, with the ratio of 5:2:3. The three subsets are finger-wise disjoint, that is all FV images corresponding to a given identity appear in only one of the three sets. This way of partitioning the data is also called subject-independent partitioning [39]. The training set is used for learning-based methods, that is, for training data-driven models; the development set is used for selecting the values of certain hyper-parameters; whereas the test set is used for testing the generalization of the method. Since the baseline method in this work is not a learning-based method, only the development set and the test set are used.

We evaluate the performance of the proposed methods by using two protocols: *balanced protocol* and *normal protocol*.

- The balanced protocol is designed to test the discrimination ability of the authentication algorithm, that is, to distinguish between genuine and impostor presentations. In this protocol the ratio of genuine to impostor presentations is 1:1. For any given finger, the maximum number of genuine comparisons can be computed as C_N^2, where C denotes the Binomial Coefficient and N denotes the number of finger presentations per finger. In our development and test sets $N = 10$.
- The normal protocol is designed to exhaustively simulate most common biometrics application scenarios where a given identity may be subject to several impostor attacks. In the normal protocol, the first sample of each finger is used as the enrolment sample, and the other nine samples are considered as probe samples. Thus, the number of impostor comparisons is much larger than the number of genuine comparisons.

Table VI summarizes the key statistics of the two protocols. The authentication score threshold is selected over the development set of each protocol and then applied to the corresponding test sets[10].

B. Criteria and Metrics

Criteria and metrics are essential for evaluating the biometrics system. To comprehensively evaluate the performance of the proposed methods, this work uses several commonly used criteria and metrics in biometrics field. The criteria are based on some metrics. Once the criteria are determined, the performance of the authentication can be evaluated by some metrics. The metrics and the criteria used in this work are described briefly below:

1) Metrics: Five metrics are used in this work: false match rate (FMR), false non match rate (FNMR), half total error rate (HTER), equal error rate (EER), and 1-FNMR. FMR indicates the proportion of impostor matches that are incorrectly accepted by the system, whereas FNMR denotes the proportion of genuine matches incorrectly rejected by the system. HTER is the mean of FMR and FNMR. EER is the error rate corresponding to the operating point (score-threshold over the development set) where FMR and FNMR are equal. 1-FNMR indicates the true matching rate; it usually used together with a fixed FMR.

2) Criteria: Three criteria are used in this work: minimum HTER (min-HTER) criterion, EER criterion, and fixed-FMR. The min-HTER criterion is used to compare experiments with different parameters, and find the parameters that lead to the lowest misclassification error; the EER criterion is used in scenarios when both FMR an FNMR are considered to be equally important; In most real-world applications, false-matches are considered to be far more important than false non-matches. In such scenarios, the biometrics system is tuned to limit the FMR to a certain acceptable value, typically 1% or even 0.1%.

C. Baseline FVA Process

In this work the maximum curvature (MC) feature extraction method and the Miura Match (MM) feature-comparison method [21] are adopted as the baseline FVA pipeline. The full-view FVA process is shown in Figure 6. Note that, in this work, the single-view FVA is a necessary step for full-view FVA. Figure 6 shows the full-view processing pipeline. For single-view FVA, the process consists in selecting the optimal input image using the FVIA algorithm, MC feature extraction, comparing the probe image to the enrolled image using the MM method, and finally thresholding the MM score to generate the authentication

[10]The dataset used, the experimental protocols, and the source-code for reproducing the experiments presented in this work shall be shared publicly for research purposes, upon publication of this work.

TABLE VI: Experimental protocols. The three subsets are finger-wise disjoint, that is all FV images corresponding to a given identity appear in only one of the three sets.

Num	Balanced protocol			Normal protocol		
	Training set	Development set	Test set	Training set	Development set	Test set
Number of identities (fingers)	160	64	96	160	64	96
Number of genuines	/	2880	4320	/	576	864
Number of impostors	/	2880	4320	/	36288	82080
Total number of comparisons	/	5760	8640	/	36864	87944

TABLE VII: Performance of FVIA with different gray thresholds. Metric used here is HTER (%), and the best result of each column is indicated in underline font, where as the global best result is indicated in the bold font. Maximum, Minimum, Mean, and Median denote the maximum value fusion, minimum value fusion, mean value fusion, and median value fusion, respectively. SVM-Linear, SVM-Poly, and SVM-RBF denote fusion by SVM with linear kernel, polynomial kernel, and RBF kernel, respectively.

Gray Threshold	Single-view			Multi-view fusion						
	View 1	View 2	View 3	Maximum	Minimum	Mean	Median	SVM-Linear	SVM-Poly	SVM-RBF
60	12.27	9.83	4.65	3.54	7.41	2.41	4.29	2.19	2.17	2.19
70	12.29	9.74	4.58	3.49	7.24	2.31	4.24	2.05	2.03	2.08
80	12.26	9.65	4.55	3.52	7.24	2.38	4.32	2.12	2.05	2.05
90	12.45	9.58	4.57	3.51	7.27	2.38	4.31	2.15	2.08	2.08
100	12.47	9.60	4.58	3.51	7.27	2.36	4.34	2.14	2.07	2.05
110	12.41	9.67	4.67	3.54	7.38	2.45	4.36	2.20	2.05	2.08
120	12.34	9.69	4.67	3.49	7.33	2.40	4.20	2.19	**1.98**	2.01
130	12.29	9.65	4.97	3.66	7.34	2.41	4.22	2.20	2.07	2.15
140	12.15	9.79	5.03	3.72	7.48	2.47	4.17	2.26	2.22	2.22
150	11.98	9.77	4.97	3.72	7.27	2.43	4.17	2.26	2.22	2.20
160	11.94	9.77	4.93	3.77	7.60	2.50	4.15	2.27	2.17	2.15
170	11.82	9.95	5.24	3.85	7.67	2.57	4.06	2.27	2.22	2.24
180	11.88	9.90	5.23	3.99	7.62	2.52	4.06	2.34	2.24	2.26
190	11.74	9.72	5.30	4.13	7.59	2.55	4.10	2.29	2.29	2.27
200	11.79	9.67	5.10	4.15	7.43	2.60	4.22	2.43	2.34	2.36

result. Then, we combine the single-view FVA scores of the three views using a suitable score-fusion method to generate the full-view FVA score and decision.

To evaluate the performance of full-view FVA, seven score-fusion methods have been used to combine the three single-view scores. The fusion methods are: maximum fusion, minimum fusion, median fusion, mean fusion and classification of a 3D score-vector using a support vector machine (SVM) with the linear kernel (SVM-Linear), polynomial kernel (SVM-Poly), and radial-basis-function kernel (SVM-RBF), respectively.

D. Illumination Adaptation Experiments

In this section the performance of the proposed FVIA algorithm is comprehensively evaluated. The purpose of FVIA is to select the FV image with best quality for each view from six FV images captured with different illumination intensities. The selected FV images should lead to the lowest possible HTER. Hence, we use the min-HTER criterion to evaluate the performance of the FVIA algorithm.

1) FVIA with different gray thresholds: As described in Section IV, the FVIA algorithm depends on a threshold T. Therefore, when applying this algorithm, the first step is to determine the appropriate value for the threshold, T. We have conducted an experiment where T is varied from 60 to 200 in intervals of 10. A total of 15 values are considered as candidate thresholds. The value of T that produces the minimum HTER is adopted as the FVIA threshold.

The results of the proposed FVIA algorithm with different

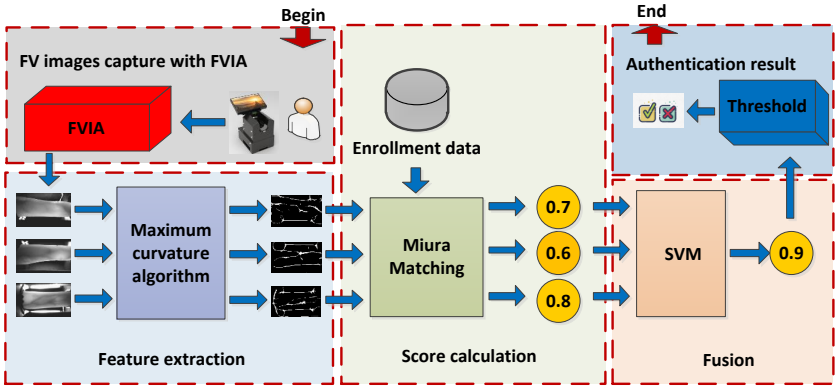

Fig. 6: Baseline full-view FVA process. The process begin at FV images capture with FVIA, FV feature extraction, score calculation, scores fusion, and end at authentication result output.

TABLE VIII: Comparison experiments of FVIA with fixed illumination intensity. Metric used here is HTER (%). The best results in each case (single-view/full-view-fusion) are indicated in bold font while the second are underlined.

Illumination	Single-view			Full-view						
	View 1	View 2	View 3	Maximum	Minimum	Mean	Median	SVM-Linear	SVM-Poly	SVM-RBF
Fixed illumination 1	14.53	10.02	5.35	4.29	8.39	3.06	4.76	2.97	2.78	2.76
Fixed illumination 2	**12.15**	10.00	**4.65**	3.63	7.78	3.06	4.31	2.52	2.34	2.31
Fixed illumination 3	12.71	11.32	4.81	3.89	10.07	4.05	5.07	2.92	2.40	2.41
Fixed illumination 4	14.11	13.32	8.28	5.66	12.60	7.29	8.07	5.95	4.39	3.91
Fixed illumination 5	14.93	13.61	9.32	6.77	14.41	8.33	8.68	7.85	5.17	4.70
Fixed illumination 6	14.18	13.58	8.73	6.49	14.17	8.37	8.54	7.71	4.98	4.65
Adaption with FVIA	12.34	**9.69**	4.67	**3.49**	**7.33**	**2.40**	**4.20**	**2.19**	**1.98**	**2.01**

TABLE IX: Comparison of FVIA with individual measures. The best results in each case (single-view/full-view) are indicated in bold font and the second-best result is underlined. The metric used here is HTER (%).

Method	Single-view			Multi-view fusion						
	View 1	View 2	View 3	Maximum	Minimum	Mean	Median	SVM-Linear	SVM-Poly	SVM-RBF
E	12.03	9.69	5.09	3.91	7.40	2.55	4.31	2.33	2.26	2.27
V	**11.93**	**9.58**	5.14	3.96	7.71	2.62	**4.20**	2.47	2.22	2.22
$\bar{G}$	14.55	13.35	9.01	6.63	14.06	8.21	8.42	7.71	5.02	4.65
FVIA (proposed)	12.34	9.69	**4.67**	**3.49**	**7.33**	**2.40**	**4.20**	**2.19**	**1.98**	**2.01**

TABLE X: Ablation experiments of FVIA. Metric used here is HTER (%). The best results in each case (single-view/full-view) are indicated in bold font while the second are underlined.

Algorithm	Single-view			Multi-view fusion						
	View 1	View 2	View 3	Maximum	Minimum	Mean	Median	SVM-Linear	SVM-Poly	SVM-RBF
Ablation of variance	12.53	**9.67**	4.81	3.58	**7.19**	2.53	4.29	2.22	2.08	2.17
Ablation of entropy	12.41	9.81	4.79	3.70	7.45	2.47	4.36	2.29	2.14	2.19
Ablation of mean gray velue	**11.88**	9.91	5.02	3.92	7.83	2.62	**4.17**	2.24	2.26	2.24
FVIA (proposed)	12.34	9.69	**4.67**	**3.49**	7.33	**2.40**	4.20	**2.19**	**1.98**	**2.01**

gray thresholds T are shown in Table VII. As the results show, the lowest overall HTER, 1.98%, occurs when $T = 120$. Therefore, in this work when computing $\mathcal{C}$, the threshold T is set to $T^* = 120$. Furthermore, observing the evolution of the HTER for the full-view case, we note that the performance drops as T tends to either end of the range (60, 200). This observation is consistent with our principle in Section IV-A that $\bar{G}$ can be used for illumination adaptation.

From Table VII we draw two further conclusions. 1) The performance of full-view fusion is better than that of any single view, which demonstrates the advantage of full-view FVA. 2) The performance of View 3 is clearly superior to that of View 1 or 2. This observation shows that in this dataset, the palmar view of the finger includes more discriminatory information than the other views. These two phenomena will be comprehensively evaluated in the authentication experiments in Section V-E.

2) Comparison of FVIA with Fixed Illumination Intensity: Next, we study the advantage of combining the MIFV strategy and the FVIA algorithm, over FVA with fixed illumination. Specifically, we compare the FVA performance when using the FVIA algorithm to the FVA scenario where all FV images are captured under only a single, fixed illumination intensity. We simulate the fixed illumination scenario by considering only images of a pre-determined illumination intensity for each finger-presentation.

Table VIII shows the experimental results of each illumination scenario. From these results we can see that in most of the cases (single-view/full-view), the proposed FVIA algorithm results in lower authentication error than when using fixed illumination. In those cases where illumination selected by FVIA are not the best, they are a close second. We conclude from these observations that the proposed FVIA algorithm can effectively reduce the FVA error rate.

3) Comparison of FVIA with individual measures: We have compared the performance of the proposed FVIA algorithm with those of the individual quality measures – entropy(E), variance (V), and mean gray value ($\bar{G}$). Table IX shows the performances of these comparison measures. In these results we see that in most cases the proposed FVIA method achieves the best results. Specifically, the FVIA algorithm achieves the best results in all of the full-view cases. The advantage of the FVIA algorithm is further demonstrated.

4) Ablation experiments for FVIA algorithm: We have also conducted ablation experiments to investigate the contribution of each component of the proposed FVIA algorithm. For the ablation of the entropy component, e^E is set to zero in the FVIA algorithm, for the ablation of the variance component, V is ignored in the FVIA algorithm, and for the ablation of $\bar{G}$, the entire denominator in Equation 2 is excluded, that is, set to 1.

The results of the FVIA ablation experiments, presented in Table X, show that in most cases (single-view as well as full-view), the performance of the complete FVIA algorithm is generally superior to that when ablating any individual measure. In all cases, the performance of the proposed FVIA algorithm is in the top two results. These ablation experiments demonstrate that all three measures contribute significantly to the performance of the FVIA algorithm.

5) Qualitative analysis of the proposed FVIA: To qualitatively analyze the proposed FVIA algorithm, the composite FVIA coefficient $\mathcal{C}$ is calculated with the illumination intensity variant from Illumination 1 (I1) to Illumination 6 (I6). For comparison, we have also calculated the individual measures

of the FVIA algorithm, the entropy, variance, and mean gray-value. The first sample of each finger are used for analysis.

Figure 7shows the box-plot of the four entities ($\mathcal{C}$, E, V, and $\bar{G}$) for each of the three views. From these plots, we can see that the discriminative power of the FVIA coefficient, $\mathcal{C}$, is superior to that of the three individual measures. Specifically, we note the following phenomena:

- Compared to entropy, the FVIA coefficient $\mathcal{C}$ not only has better discriminative power, but also more obvious trend of change, for example, the median changes more significantly with illumination intensities.
- Compared to variance, the composite FVIA coefficient $\mathcal{C}$ tends to select images recorded using lower illumination intensity. This is a result of including the mean gray-value in C. Combining this phenomenon with the results in Section V-D3, we analyze that the proposed FVIA coefficient $\mathcal{C}$ can avoid overexposure due to high illumination intensity.
- Compared to the mean gray-value, The FVIA coefficient has low value when the illumination intensity is either too weak or too strong, so as to avoid under-exposure or over-exposure. This is consistent with the theoretical expectations as described in Section IV.

E. Finger Vein Authentication Experiments

In this section we provide baseline FVA results for the MFFV-N dataset. The process of FV baseline authentication is shown in Figure 6. To comprehensively evaluate the FVA performances of the MFFV-N dataset, we use three performance criteria in the FVA experiments: EER, min-HTER, and fixed FMR (in this work, both FMR=1% and FMR=0.1% have been used). These criteria cover most of the common application scenarios for FVA. In all these experiments the authentication score threshold is selected over the development set of the selected protocol and then applied to the corresponding test set.

1) Single-View FVA: The proposed MFFV device can also be used for single-view FVA, where each view is considered individually. The FVA results are presented in Table XI. Score distributions for genuine and impostor matches (represented by probability densities expressed as percentages) are shown in Figure 8(a) to 8(f).

From Table XI we see that, for both protocols, FV samples from View 3 consistently produce the better performance than those of View 1 and 2. This conclusion is also evident from Figure 8(a) to 8(f) where we see that the zero effort impostor (ZEI) score distribution (blue) and the genuine-score distribution (green) are best separated for View 3. Therefore, we can conclude that, for the MFFV-N dataset, the palmar view of finger includes more discriminatory FV information than the other two views. In some cases, namely, the fixed FMR criteria, we note that the results of View 1 and 2 are better than that of View 3. However, in these cases the corresponding FNMR (and consequently, HTER) are much higher than the corresponding values for View 3. This means that in these

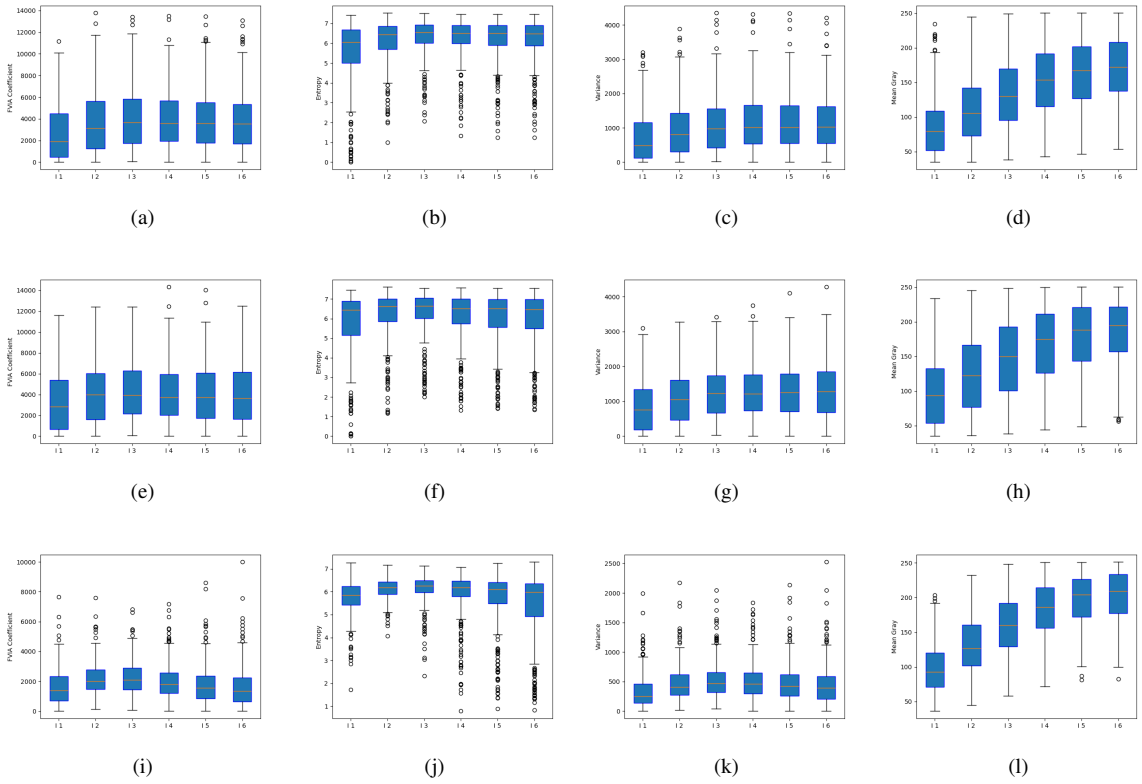

Fig. 7: Qualitative analysis of FVIA coefficient and individual measures comparison. (a)-(d), (e)-(h), and (i)-(l) shown the qualitative analysis results of View 1, View 2, and View 3 respectively, in the order of FVIA coefficient, entropy, variance and mean gray value.

TABLE XI: Authentication performance of each single view, and full-view. The best results are indicated in bold font, and the second best results are underlined.

Criterion	View	Balanced protocol							Normal protocol						
		Development set				Test set			Development set				Test set		
		EER	FMR	FNMR	HTER	FMR	FNMR	HTER	EER	FMR	FNMR	HTER	FMR	FNMR	HTER
EER	View 1	12.78	12.78	12.78	12.78	10.32	13.56	11.94	17.02	17.02	17.01	17.02	13.70	18.63	16.17
	View 2	10.35	10.35	10.35	10.35	6.88	14.81	10.84	15.31	15.34	15.28	15.31	11.13	22.11	16.62
	View 3	5.17	5.17	5.17	5.17	5.74	7.71	6.72	8.30	8.26	8.33	8.30	7.13	14.35	10.74
	Full-view	**2.08**	**2.08**	**2.08**	**2.08**	**2.29**	**4.51**	**3.40**	**3.97**	**3.94**	**3.99**	**3.97**	**2.32**	**8.56**	**5.44**
		EER	FMR	FNMR	HTER	FMR	FNMR	HTER	EER	FMR	FNMR	HTER	FMR	FNMR	HTER
min-HTER	View 1	/	8.30	16.39	12.34	6.76	16.81	11.78	/	10.12	21.88	16.00	7.90	24.07	15.99
	View 2	/	6.49	12.88	9.69	4.47	17.48	10.97	/	9.73	19.62	14.67	6.73	26.27	16.50
	View 3	/	2.47	6.88	4.67	3.36	10.16	6.76	/	5.83	9.38	7.60	4.94	17.36	11.15
	Full-view	/	**1.77**	**2.19**	**1.98**	**2.08**	**4.65**	**3.37**	/	**2.97**	**4.34**	**3.66**	**1.67**	**9.72**	**5.69**
		1-FNMR	FMR	FNMR	HTER	FMR	FNMR	HTER	1-FNMR	FMR	FNMR	HTER	FMR	FNMR	HTER
FMR=1%	View 1	64.90	**0.97**	35.10	18.04	**0.65**	33.73	17.19	53.30	**1.00**	46.70	23.85	0.82	43.63	22.23
	View 2	71.91	**0.97**	28.09	14.53	**0.65**	34.49	17.57	53.82	**1.00**	46.18	23.59	0.64	51.39	26.02
	View 3	89.55	**0.97**	10.45	5.71	1.76	16.04	8.90	77.78	**1.00**	22.22	11.61	0.86	30.67	15.77
	Full-view	**96.39**	**0.97**	**3.61**	**2.29**	1.34	**6.25**	**3.80**	**89.93**	**1.00**	**10.07**	**5.53**	**0.49**	**15.74**	**8.12**
		1-FNMR	FMR	FNMR	HTER	FMR	FNMR	HTER	1-FNMR	FMR	FNMR	HTER	FMR	FNMR	HTER
FMR=0.1%	View 1	42.01	0.07	57.99	29.03	0.02	54.98	27.50	33.33	**0.10**	66.67	33.38	0.08	61.57	30.83
	View 2	42.81	0.07	57.19	28.63	**0.00**	68.03	34.02	34.38	**0.10**	65.63	32.86	**0.06**	76.04	38.05
	View 3	75.90	0.07	24.10	12.08	0.28	32.34	16.31	58.51	**0.10**	41.49	20.80	0.07	50.46	25.27
	Full-view	**92.05**	**0.07**	**7.95**	**4.01**	0.35	**11.92**	**6.13**	79.51	**0.10**	**20.49**	**10.29**	**0.06**	**27.20**	**13.63**

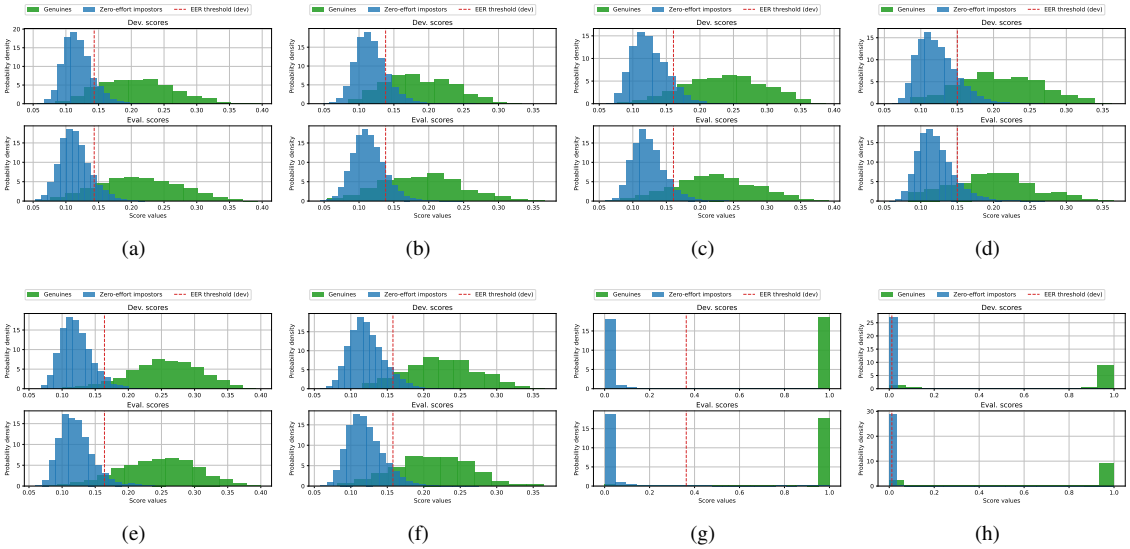

Fig. 8: FVA score distributions. The red dotted line indicates where the threshold is selected (on development set) with EER criterion. (a), (b): Score-distributions of View 1 with balanced protocol and normal protocol, respectively; (c), (d): Score-distributions of View 2 with balanced protocol and normal protocol, respectively; (e), (f): Score-distributions of View 3 with balanced protocol and normal protocol, respectively; (g), (h) Score-distributions of full-view FVA for balanced protocol and normal protocol, respectively.

tests, although the FMR values for View 3 are slightly worse than those of Views 1 and 2, the overall performance for View 3 is still significantly better.

2) Full-View FVA Experiments: The baseline full-view FVA method follows a score-fusion approach, based on the three single-view FVA scores. As depicted in Figure 6, in addition to the processes of the single-view FVA, the full-view FVA includes a score fusion process. Based on the results presented in Table VII, we adopt the SVM with polynomial kernel (SVM-Poly) for fusing the scores of the three views.

For ease of comparison with single-view FVA, the full-view FVA results are also presented in Table XI. Figure 8(g) to 8(h) show the genuine and ZEI score distributions for full-view FVA. For EER criterion, the EER of development set is 2.08% in the balanced protocol and 3.97% in the normal protocol.

For min-HTER criterion, in the balanced protocol we reach an HTER of 1.98% for development set and 3.37% for test set. Correspondingly, in the normal protocol we see a min-HTER of 3.66% for the development set 5.69% for the test.

For fixed FMR criterion, on development sets, the (1-FNMR)@FMR=1% metric achieves 96.39% and 89.93%, and the HTER metric ahiceves 2.29%, and 5.53%, in the balanced protocol and the normal protocol, respectively. Under this criterion, on test set, the HTER achieves 3.80% (balanced protocol) and 8.12% (normal protocol), respectively. When FMR is limited to 0.1%, on development set, the (1-FNMR)@FMR=0.1% metric comes to 92.05% and 79.51%, and the HTER metrics comes to 4.01% and 10.29% for the balanced

TABLE XII: Examples of the LFMB-3DFB dataset.

	Capture 1	Capture 2	Capture 3	Capture 4	Capture 5	Capture 6
View A	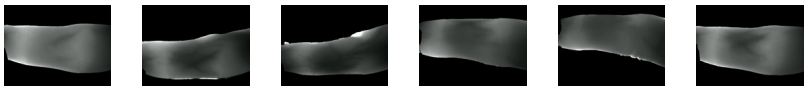					
View C	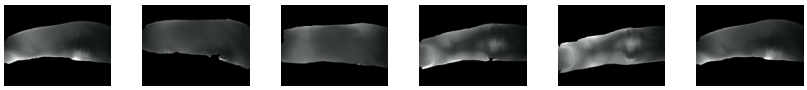					
View E	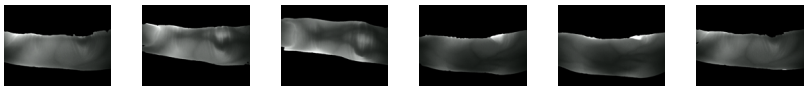					

TABLE XIII: Comparison with LFMB-3DFB (%).

Criterion	Method	Balance protocol						
		Development set				Test set		
EER	MC+MM+SVM	EER 35.38	FMR 35.38	FNMR 35.38	HTER 35.38	FMR 32.93	FNMR 35.23	HTER 34.08
min-HTER	MC+MM+SVM	EER /	FMR 13.61	FNMR 52.69	HTER 33.15	FMR 13.04	FNMR 53.33	HTER 33.18
FMR=1%	MC+MM+SVM	1-FNMR 25.15	FMR 0.99	FNMR 74.85	HTER 37.92	FMR 0.72	FNMR 74.75	HTER 37.74
FMR=0.1%	MC+MM+SVM	1-FNMR 18.10	FMR 0.10	FNMR 81.90	HTER 41.00	FMR 0.07	FNMR 81.81	HTER 40.94

and normal protocols, respectively. The corresponding HTER values (test set) obtained are 6.13% and 13.63%, respectively, for the two protocols.

Compared to the results of single-view, there is significant improvement in full-view FVA. Figure 8(g) to 8(h) shows a clear separation between genuine matches and ZEI matches for full-view FVA. The separation between the two classes is significantly higher for full-view FVA than for the single-view case (compare with Figure 8(g) to 8(h).) In particular, note that the (1-FNMR) values for the fixed FMR criteria are much higher for the full-view authentication than for those of any single-view authentication case. These results demonstrate the significant advantage of full-view over single-view FVA.

F. Time Complexity Experiments

To evaluate the time complexity of the proposed FVIA method, we estimate the time required when using FVIA algorithm in this experiment. The time complexity of the FVIA algorithm is the time for obtaining the optimally illuminated FV image from the six images captured with different illumination intensities. In addition, we also estimate the time required for the other processing, including MC feature extraction, MM score calculation, and SVM fusion, thus providing a benchmark (Note that here we only discuss the time for using this dataset; for the time of imaging, please see Section III) for future works that use our MFFV dataset. The time complexity experiments are conducted on the WSL (Windows Subsystem for Linux) system with the Intel Core i7-14700HX processor and 32G 5600MT/s DDR5 (Double Data Rate Fifth Generation) RAM (Random Access Memory).

Table XIV shows the time required for each process for each process. To provide an intuitive idea about the relative computational costs of the various steps in the processing pipeline, we also provide the proportion of time (expressed as a percentage) consumed by each step. The numbers (time required for FVIA, MC feature extraction, and MM score calculation) shown in Table XIV are for single-view processing. For full-view processing, the time required is three times the time required for single-view processing. The additional time required for SVM-based score-fusion in full-view FVA is very short compared to the time required for computing the three single-view match-scores. From the table we can see that the time complexity of the FVIA algorithm is quite short compared to the feature-extraction process. In other words, the FVIA algorithm proposed here adds a relatively short time complexity to the processing pipeline, while providing better FVA performance. From these experimental results, we can see that the time cost proportion of the proposed FVIA algorithm is quite small compared to the feature extraction process. In other words, the FVIA algorithm proposed in this work uses relatively low time cost to obtain better authentication performance.

TABLE XIV: Time Complexity Test

Process	**Time (ms)**	**Proportion**
FVIA	44.55	7.33%
MC Feature Extraction	560.90	92.29%
MM Score Calculation	2.15	0.35%
SVM Fusion	0.14	0.02%
Total	607.74	100%

G. Comparison with LFMB-3DFB Dataset

To the best of our knowledge, only one other multi-camera based full-view FV dataset has been published – the LFMB-3DFB dataset [19]. In this section we study the performance

of our baseline full-view FVA method on the LFMB-3DFB dataset. The LFMB-3DFB dataset has been collected using a full-view FV device with six cameras (named 'A' to 'F') in a hexagonal configuration. For fair comparison with the proposed MFFV dataset, in this experiment we have selected only three of the six views in the LFMB-3DFB dataset – views A, C, and E, as shown in Table XII. The experiment is conducted with the protocol provided by the LFMB-3DFB dataset, which is similar to the balanced protocol of the proposed MFFV dataset.

Table XIII shows the FVA results for the LFMB-3DFB dataset. Comparing this table with Table XI, it is clear that the full-view authentication results for the LFMB-3DFB dataset are significantly worse than those for the MFFV dataset. The reason for the poor full-view FVA performance on the LFMB-3DFB dataset in this experiment lies in the way the data was collected. During data-collection of the LFMB-3DFB dataset, the volunteers were asked to place the finger in the device at an arbitrary angle for each presentation. As a result, in this dataset, different presentations of the same finger have been imaged at different orientations, as shown in Table XII. In other words, for two presentations of the same finger, the images from a given camera may not capture the same view of the finger. This intra-class finger-orientation variation does not affect the FVA performance when all six views are considered together. However, for single-view FVA, the difference in orientation between the enrolled FV sample and the probe FV sample may lead to a mismatch in a genuine comparison. Indeed, in Table XIII we see that the FNMR is extremely high for the min-HTER and fixed FMR criteria. From this experiment we conclude that the LFMB-3DFB dataset may be used for full-view FVA based on all six views taken together, but the dataset is not very suitable for single-view authentication, or full-view authentication based on score-fusion of single-view FVA. Note that the FVIA algorithm is not applicable to the LFMB-3DFB dataset, because a constant illumination intensity has been used for all presentations in this dataset.

VI. Conclusions and Future Work

In this work we have presented the design of a new full-view FV biometrics device, named MFFV. The MFFV device incorporates a novel mirror-based image-capture mechanism, to increase the distance between the target (finger) and the camera without sacrificing compactness. We propose a two-step approach to obtain optimally illuminated images for fingers with different thicknesses. The first step involves the proposed MIFV imaging strategy, where six images with varying illumination intensities are recorded for every sample, in each view of the finger. To complement the MIFV capture strategy, we propose a novel FVIA algorithm that selects, during processing, the optimal image from the six MIFV images. The combination of the MIFV imaging strategy and FVIA algorithm not only addresses the issue of selecting the optimal illumination intensity for fingers of varying thicknesses, but also helps to reduce the cost of the device (by compensating for lower-quality cameras) while maintaining high FVA performance.

Using the MFFV device, we have curated a new full-view FV dataset, named the MFFV dataset. This dataset has 172,800 FV images corresponding to 320 fingers. This full-view, multi-illumination-intensity, multi-orientation FV dataset can support FV research in many directions, thus promoting the advancement of FV biometrics. In this work, we have used only a portion of the MFFV dataset, named MFFV-N, which is publicly available for research purposes[1]. The effectiveness of the proposed FVIA algorithm is evaluated and demonstrated by the extensive experiments on the MFFV-N dataset.

Finally, we present a set of baseline FVA results for the MFFV-N dataset using two experimental protocols, which simulate most of the common biometrics application scenarios. In our baseline FVA process, first the MIFV strategy is used to record multiple FV images of the presented finger, and the FVIA algorithm is applied to select the optimal probe FV image from this set. Then the maximum-curvature (MC) method is used to create a template of vein-features. The probe template is compared to the corresponding enrolment template using the Miura-Match (MM) method, to compute a single-view match-score for each view. The single-view match-scores of the three views of the MFFV device are finally fused using a polynomial SVM classifier, to generate a full-view FVA score for the presented finger. Our experiments show that the full-view FVA is significantly better than any single-view authentication performance.

In future we plan to extend our work in both directions, software and hardware. In terms of FVA software, we will develop deep-learning based methods for end-to-end full-view FVA. We also plan to make further improvements to the proposed device. In particular we plan to expand the illumination range, by adding not only more intensity-levels, but also including additional wavelengths for illumination. In the current version of the MFFV device the range of illumination intensities is the same for all three views. Our experience in this work shows that this setup is still not the best. Because the cross-section of the finger is more oval than circular, we believe that the range of illumination intensities should different for the different views.

References

[1] L. Yang, X. Liu, G. Yang, J. Wang, and Y. Yin, "Small-area finger vein recognition," *IEEE Transactions on Information Forensics and Security*, vol. 18, pp. 1914–1925, 2023.

[2] L. Yang, G. Yang, K. Wang, F. Hao, and Y. Yin, "Finger vein recognition via sparse reconstruction error constrained low-rank representation," *IEEE Transactions on Information Forensics and Security*, vol. 16, pp. 4869–4881, 2021.

[3] S. Li, R. Ma, L. Fei, and B. Zhang, "Learning compact multirepresentation feature descriptor for finger-vein recognition," *IEEE Transactions on Information Forensics and Security*, vol. 17, pp. 1946–1958, 2022.

[4] A. Krishnan, T. Thomas, and D. Mishra, "Finger vein pulsation-based biometric recognition," *IEEE Transactions on Information Forensics and Security*, vol. 16, pp. 5034–5044, 2021.

[5] J. Huang, W. Luo, W. Yang, A. Zheng, F.-Z. Lian, and W. Kang, "Fvt: Finger vein transformer for authentication," *IEEE Transactions on Instrumentation and Measurement*, vol. 71, pp. 1–13, 2022.

[6] W. Yang, C. Hui, Z. Chen, J.-H. Xue, and Q. Liao, "Fv-gan: Finger vein representation using generative adversarial networks," *IEEE Transactions on Information Forensics and Security*, vol. 14, pp. 2512–2524, 2019.

[7] J. Huang, M. Tu, W. Yang, and W. Kang, "Joint attention network for finger vein authentication," *IEEE Transactions on Instrumentation and Measurement*, vol. 70, pp. 1–11, 2021.

[8] F.-Z. Lian, J.-D. Huang, J.-X. Liu, G. Chen, J.-H. Zhao, and W.-X. Kang, "Fedfv: A personalized federated learning framework for finger vein authentication," *Machine Intelligence Research*, pp. 1–14, 2023.

[9] A. Uhl, C. Busch, S. Marcel, and R. Veldhuis, *Handbook of vascular biometrics*. Springer Nature, 2020.

[10] J. Huang, A. Zheng, M. S. Shakeel, W. Yang, and W. Kang, "Fvfsnet: Frequency-spatial coupling network for finger vein authentication," *IEEE Transactions on Information Forensics and Security*, vol. 18, pp. 1322–1334, 2023.

[11] S. Li and B. Zhang, "Joint discriminative sparse coding for robust hand-based multimodal recognition," *IEEE Transactions on Information Forensics and Security*, vol. 16, pp. 3186–3198, 2021.

[12] S. Li, B. Zhang, L. Fei, S. Zhao, and Y. Zhou, "Learning sparse and discriminative multimodal feature codes for finger recognition," *IEEE Transactions on Multimedia*, vol. 25, pp. 805–815, 2023. [Online]. Available: https://api.semanticscholar.org/CorpusID:244862174

[13] S. Li, B. Zhang, L. Fei, and S. Zhao, "Joint discriminative feature learning for multimodal finger recognition," *Pattern Recognit.*, vol. 111, p. 107704, 2021. [Online]. Available: https://api.semanticscholar.org/CorpusID:225110251

[14] W. Kang, H. Liu, W. Luo, and F. Deng, "Study of a full-view 3d finger vein verification technique," *IEEE Transactions on Information Forensics and Security*, vol. 15, pp. 1175–1189, 2020.

[15] S. Rozendal, "Redesign of a finger vein scanner," 2018. [Online]. Available: https://api.semanticscholar.org/CorpusID:69287982

[16] P. Zhao, S. Zhao, L. Chen, W. Yang, and Q. Liao, "Exploiting multiperspective driven hierarchical content-aware network for finger vein verification," *IEEE Transactions on Circuits and Systems for Video Technology*, vol. 32, pp. 7938–7950, 2022.

[17] B. Prommegger, C. Kauba, and A. Uhl, "Multi-perspective finger-vein biometrics," *2018 IEEE 9th International Conference on Biometrics Theory, Applications and Systems (BTAS)*, pp. 1–9, 2018.

[18] H. Qin, R. Hu, M. A. El-Yacoubi, Y. Li, and X. Gao, "Local attention transformer-based full-view finger-vein identification," *IEEE Transactions on Circuits and Systems for Video Technology*, 2022.

[19] W. Yang, Z. Chen, J. Huang, and W. Kang, "A novel system and experimental study for 3d finger multibiometrics," *IEEE Transactions on Biometrics, Behavior, and Identity Science*, vol. 4, pp. 471–485, 2022.

[20] C. Kauba, M. Drahanský, M. Nováková, A. Uhl, and S. Rydlo, "Three-dimensional finger vein recognition: A novel mirror-based imaging device," *Journal of Imaging*, vol. 8, 2022.

[21] N. Miura, A. Nagasaka, and T. Miyatake, "Extraction of finger-vein patterns using maximum curvature points in image profiles," *IEICE Trans. Inf. Syst.*, vol. 90-D, pp. 1185–1194, 2007.

[22] N. M. a, A. Nagasaka, and T. Miyatake, "Feature extraction of finger-vein patterns based on repeated line tracking and its application to personal identification," *Machine Vision and Applications*, vol. 15, pp. 194–203, 2004.

[23] B. Huang, Y. Dai, R. Li, D. Tang, and W. Li, "Finger-vein authentication based on wide line detector and pattern normalization," *2010 20th International Conference on Pattern Recognition*, pp. 1269–1272, 2010.

[24] S. Li and B. Zhang, "An adaptive discriminant and sparsity feature descriptor for finger vein recognition," *ICASSP 2021 - 2021 IEEE International Conference on Acoustics, Speech and Signal Processing (ICASSP)*, pp. 2140–2144, 2021. [Online]. Available: https://api.semanticscholar.org/CorpusID:235771223

[25] Z. Zhang and M. Wang, "Finger vein recognition based on lightweight convolutional attention model," *IET Image Process.*, vol. 17, pp. 1864–1873, 2023. [Online]. Available: https://api.semanticscholar.org/CorpusID:257034829

[26] W. Liu, H. Lu, Y. Wang, Y. Li, Z. Qu, and Y. Li, "Mmran: A novel model for finger vein recognition based on a residual attention mechanism," *Applied Intelligence*, vol. 53, pp. 3273–3290, 2022. [Online]. Available: https://api.semanticscholar.org/CorpusID:249110377

[27] B. Hou and R. Yan, "Convolutional autoencoder model for finger-vein verification," *IEEE Transactions on Instrumentation and Measurement*, vol. 69, pp. 2067–2074, 2020. [Online]. Available: https://api.semanticscholar.org/CorpusID:195428444

[28] R. S. Kuzu, E. Piciucco, E. Maiorana, and P. Campisi, "On-the-fly finger-vein-based biometric recognition using deep neural networks," *IEEE Transactions on Information Forensics and Security*, vol. 15, pp. 2641–2654, 2020. [Online]. Available: https://api.semanticscholar.org/CorpusID:212648315

[29] R. Das, E. Piciucco, E. Maiorana, and P. Campisi, "Convolutional neural network for finger-vein-based biometric identification," *IEEE Transactions on Information Forensics and Security*, vol. 14, pp. 360–373, 2019.

[30] L. Yang, G. Yang, Y. Yin, and X. Xi, "Finger vein recognition with anatomy structure analysis," *IEEE Transactions on Circuits and Systems for Video Technology*, vol. 28, no. 8, pp. 1892–1905, 2017.

[31] L. Yang, G. Yang, Y. Yin, and R. Xiao, "Finger vein image quality evaluation using support vector machines," *Optical Engineering*, vol. 52, 2013.

[32] J. Peng, Q. Li, and X. Niu, "A novel finger vein image quality evaluation method based on triangular norm," *2014 Tenth International Conference on Intelligent Information Hiding and Multimedia Signal Processing*, pp. 239–242, 2014.

[33] H. Ma, K. jun Wang, L. Fan, and F. Cui, "A finger vein image quality assessment method using object and human visual system index," in *Sino-foreign-interchange Workshop on Intelligent Science and Intelligent Data Engineering*, 2012.

[34] K. Shaheed and I. Qureshi, "A hybrid proposed image quality assessment and enhancement framework for finger vein recognition," *Multimedia Tools and Applications*, 2022.

[35] K. Shaheed, L. Yang, G. Yang, I. Qureshi, and Y. Yin, "Novel image quality assessment and enhancement techniques for finger vein recognition," *2018 International Conference on Security, Pattern Analysis, and Cybernetics (SPAC)*, pp. 223–231, 2018.

[36] M. Elderen, "Designing a stand alone finger vein scanner," B.S. thesis, University of Twente, 2022.

[37] T. D. Nguyen, Y. H. Park, K. Y. Shin, and K. R. Park, "New finger-vein recognition method based on image quality assessment," *KSII Trans. Internet Inf. Syst.*, vol. 7, pp. 347–365, 2013.

[38] H. Qin and M. A. El-Yacoubi, "Deep representation for finger-vein image-quality assessment," *IEEE Transactions on Circuits and Systems for Video Technology*, vol. 28, pp. 1677–1693, 2018.

[39] M. Wang and W. Deng, "Deep face recognition: A survey," *Neurocomputing*, vol. 429, pp. 215–244, 2018. [Online]. Available: https://api.semanticscholar.org/CorpusID:4951598

Junduan Huang is currently an associate researcher in School of Artificial Intelligence, South China Normal University, Foshan, China. He received the B.S. degree and M.S. degree from South China Agriculture University, Guangzhou, China, in 2017 and 2020, respectively, and the Ph.D degree in South China University of Technology, Guangzhou, China, in 2024, respectively. From 2022 to 2023, he was a research intern in Idiap Research Insititute, Martigny, Switzerland. His research interests include biometrics, computer vision, audio signal processing, deep learning and agricultural engineering.

Zifeng Li received the B.S. degree from South China University of Technology, Guangzhou, China, in 2022. He is currently pursuing the M.E. degree with the School of Automation Science and Engineering, South China University of Technology, Guangzhou, China. His research interests include biometrics, pattern recognition, computer vision and deep learning.

Sushil Bhattacharjee is a member of the Biometrics Security and Privacy Group at the Idiap Research Institute, where he works on biometrics recognition and presentation attack detection problems for a variety of biometrics modalities. His academic interests include signal processing and computer vision. He received a Ph.D. degree from the School of Communication Systems at the École Polytechnique Fédérale de Lausanne (EPFL) in 1999.

Sébastien Marcel heads the Biometrics Security and Privacy group at Idiap Research Institute (Switzerland) and conducts research on face recognition, speaker recognition, vein recognition, attack detection (presentation attacks, morphing attacks, deepfakes) and template protection. He received his Ph.D. degree in signal processing from Université de Rennes I in France (2000) at CNET, the research center of France Telecom (now Orange Labs). He is Professor at the University of Lausanne (School of Criminal Justice) and a lecturer at the École Polytechnique Fédérale de Lausanne. He is also the Director of the Swiss Center for Biometrics Research and Testing, which conducts certifications of biometric products.

Wenxiong Kang received the M.S. degree from Northwestern Polytechnical University, Xi'an, China, in 2003, and the Ph.D. degree from the South China University of Technology, Guangzhou, China, in 2009. He is currently a Professor with the School of Automation Science and Engineering, South China University of Technology. His research interests include biometrics, image processing, pattern recognition, and computer vision.